Geophysical Journal International

Geophys. J. Int. (2018) **213,** 1402–1411
Advance Access publication 2018 February 23
GJI Marine geosciences and applied geophysics

doi: 10.1093/gji/ggy067

Gaining insight into the T_2^*–T_2 relationship in surface NMR free-induction decay measurements

Denys Grombacher and Esben Auken

Hydrogeophysics Group, Geoscience Department, Aarhus University, DK-8000 Aarhus, Denmark. E-mail: denys.grombacher@geo.au.dk

Accepted 2018 February 22. Received 2018 February 15; in original form 2017 October 22

SUMMARY

One of the primary shortcomings of the surface nuclear magnetic resonance (NMR) free-induction decay (FID) measurement is the uncertainty surrounding which mechanism controls the signal's time dependence. Ideally, the FID-estimated relaxation time T_2^* that describes the signal's decay carries an intimate link to the geometry of the pore space. In this limit the parameter T_2^* is closely linked to a related parameter T_2, which is more closely linked to pore-geometry. If $T_2^* \simeq T_2$ the FID can provide valuable insight into relative pore-size and can be used to make quantitative permeability estimates. However, given only FID measurements it is difficult to determine whether T_2^* is linked to pore geometry or whether it has been strongly influenced by background magnetic field inhomogeneity. If the link between an observed T_2^* and the underlying T_2 could be further constrained the utility of the standard surface NMR FID measurement would be greatly improved. We hypothesize that an approach employing an updated surface NMR forward model that solves the full Bloch equations with appropriately weighted relaxation terms can be used to help constrain the T_2^*–T_2 relationship. Weighting the relaxation terms requires estimating the poorly constrained parameters T_2 and T_1; to deal with this uncertainty we propose to conduct a parameter search involving multiple inversions that employ a suite of forward models each describing a distinct but plausible T_2^*–T_2 relationship. We hypothesize that forward models given poor T_2 estimates will produce poor data fits when using the complex-inversion, while forward models given reliable T_2 estimates will produce satisfactory data fits. By examining the data fits produced by the suite of plausible forward models, the likely T_2^*–T_2 can be constrained by identifying the range of T_2 estimates that produce reliable data fits. Synthetic and field results are presented to investigate the feasibility of the proposed technique.

Key words: Hydrogeophysics.

INTRODUCTION

The surface nuclear magnetic resonance (NMR) method measures the properties of a magnetization present at depth that originates from the immersion of hydrogen nuclei within the Earth's magnetic field. To conduct a surface NMR measurement strong oscillatory currents are pulsed in a large coil (typically 25–100 m in dimension) at the ground surface in order to perturb the magnetization out of its equilibrium orientation. The surface coil is then used to measure the return of the magnetization to equilibrium, which produces a measureable voltage in the surface coil where the observed voltage is representative of the magnetization transverse to the direction of the Earth's magnetic field. Two attractive features of the surface NMR measurement are its direct sensitivity to water content (Legchenko & Shushakov 1998) and potential to gain insight into aquifer properties such as pore-size and permeability (Schirov *et al.* 1991; Mohnke & Yaramanci 2008). Direct sensitivity to water content stems from the direct proportionality of the surface NMR signal amplitude to the amount of hydrogen nuclei within the sensitive volume of the measurement, thus allowing quantitative estimation of water content without requiring calibration or empirical rock physics relationships (Legchenko & Valla 2002). The link between the surface NMR measurement and pore sizes/permeability is predicated upon the assumption that the time-dependence of the NMR signal (i.e. the parameters governing the time dependence, called relaxation times) carries an intimate link with the geometry of the pore space (Kenyon *et al.* 1988). The link between relaxation times and pore geometry can be demonstrated analytically (Brownstein & Tarr 1979), and many NMR studies have demonstrated that the link between relaxation times and pore geometry is robust in practice (Howard & Kenyon 1992; Straley *et al.* 1997). However, much of the studies linking relaxation times and pore geometry involve the relaxation times T_1 and T_2. The standard surface NMR measurement, called a free-induction decay (FID), measures a different relaxation time called the effective transverse relaxation time T_2^*. Although T_2^* is related to T_2 (and therefore carries information about pore geometry), T_2^* is also more strongly influenced by an additional mechanism arising due to the presence of background magnetic field inhomogeneity (Grunewald & Knight 2011). This additional contribution to T_2^* can mask its sensitivity to the pore geometry. The challenge is that the relationship between T_2^* and T_2 is unknown; that is, it is highly uncertain whether T_2^* is a reliable indicator of pore geometry or if it has been contaminated by background magnetic field inhomogeneity given only FID measurements.

The uncertainty about which mechanism controls T_2^* is the motivating factor behind the development of several alternative surface NMR transmit schemes (Legchenko *et al.* 2004; Legchenko *et al.* 2010; Walbrecker *et al.* 2011; Grunewald & Walsh 2013; Grunewald *et al.* 2014), that aim to directly measure T_1 or T_2; thus strengthening the link to pore geometry. These approaches provide the advantage that they either greatly reduce or are not sensitive to the impact of background magnetic field inhomogeneity. Two of these approaches, the spin-echo (Legchenko *et al.* 2010) and pseudo-saturation recovery approach (Walbrecker *et al.* 2011) require significant increases in survey times due to the need to build the observed decays point by point. The multi-echo approach (Grunewald & Walsh 2013) can sample the T_2 decay at multiple times during a single measurement and therefore does not require an increase in survey times. However, the multi-echo approach has reduced depth penetration because it is forced to split the energy stored in a capacitor bank into several pulses (typically 3–6 pulses). Despite the successes of these methods, the FID remains a staple measurement in surface NMR because it is one of the fastest measurements to collect, provides the greatest depth penetration, and can produce robust estimates of the subsurface water content profile. If the relationship between T_2^* and T_2 could be constrained from FID data alone it would greatly enhance the utility of the surface NMR FID measurement.

We investigate the hypothesis that relaxation during pulse (RDP) effects can be used to gain insight into the relationship between T_2^* and T_2. An updated surface NMR forward model that solves the full Bloch equation with appropriately weighted relaxation terms present (Grombacher *et al.* 2017) is used to test whether the range of T_2 consistent with the observed data can be restricted using only FID data. Grombacher *et al.* (2017) propose to weight the relaxation terms present in the Bloch equation using the observed T_2^* values. This approach differs from the standard surface NMR forward model, which neglects the relaxation terms in the Bloch equation. However, solving the full Bloch equation requires an assumption to be made about the magnitude of T_2 and T_1, both of which can only be constrained to be greater than or equal to T_2^* if given only FID data. To address this uncertainty we propose to conduct a parameter search where inversions are performed using a range of forward models, each solving the full Bloch equations for a distinct but plausible T_2 magnitude. The idea behind the proposed method is that allowing the forward model to reflect the impact of RDP on the signal amplitude, phase, and spatial origin for a particular T_2^*–T_2 pair may help improve the fit to complex-valued surface NMR data. If satisfactory data fits can only be produced given reliable T_2 estimates it would provide valuable insight into the underlying T_2^*–T_2 relationship. At minimum, we aim to narrow the range of plausible T_2 values consistent with the data. If feasible, this approach may offer great potential to improve the utility of the FID for estimations of pore-scale properties. Synthetic and field results are presented to investigate whether such an approach can be used to better constrain the relationship between T_2^* and T_2.

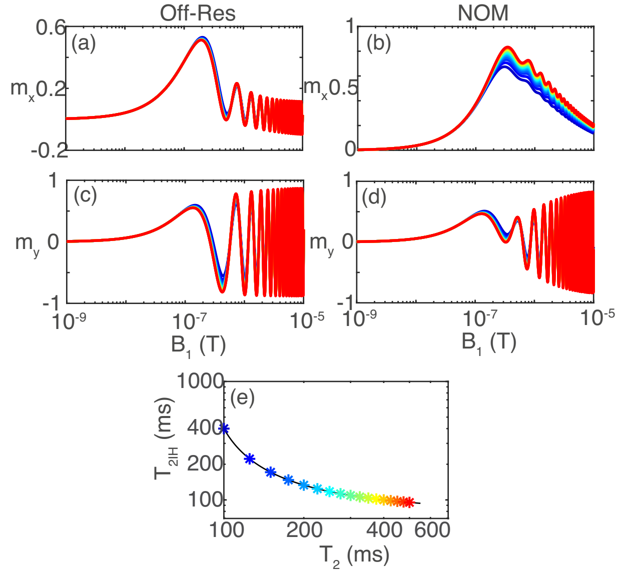

Figure 1. The m_x (top row) and m_y (middle row) components produced by two example excitation pulses. The left and right columns correspond to a 4 Hz 40 ms off-resonance pulse and an example NOM adiabatic half passage pulse, respectively. The profile colours in each case correspond to a particular T_2–T_{2IH} combination (always consistent with $T_2^* = 80$ ms). The relevant profile colour for each T_2–T_{2IH} pair is indicated by the star of the same colour in panel (e). (e) The T_2^* contour illustrating a range of plausible T_2–T_{2IH} pairs consistent with $T_2^* = 80$ ms. Note that the axes are logarithmic in panel (e).

BACKGROUND

The time dependence of the FID measurement is governed by the relaxation time T_2^*, where

$$\frac{1}{T_2*} = \frac{1}{T_2} + \frac{1}{T_{2IH}}. \tag{1}$$

T_2 is the term carrying the link to pore geometry, while T_{2IH} describes signal loss due to dephasing in the presence of an inhomogeneous background magnetic field (Chen *et al.* 2005; Grunewald & Knight 2011). Given that only T_2^* can be observed from FID data, there exists ambiguity about the relative magnitudes of T_2 and T_{2IH}. An observation of T_2^* is not enough to independently constrain the magnitude of T_2 and T_{2IH}. This highlights the chief difficulty interpreting the meaning of T_2^*, ideally T_2^* is strongly linked to T_2 and therefore pore geometry but we cannot be certain. Fig. 1(e) highlights this ambiguity, where the range of T_2–T_{2IH} pairs consistent with an example T_2^* of 80 ms is shown. In this T_2–T_{2IH} model space (Fig. 1e) the observed magnitude of T_2^* defines a contour of plausible scenarios (that lie on the black line), where there remains uncertainty about the location of the true scenario (i.e. which dot on the contour represents the true conditions).

Grombacher *et al.* (2017) highlight that for typical surface NMR conditions the impact of RDP effects, which describe the impact of relaxation processes on the ability of the excitation pulse to generate a measureable signal, can vary for a particular T_2^* depending on the relative magnitude of T_2 and T_{2IH}. Fig. 1 highlights the variable magnitude of RDP for a given T_2^* for two example pulse types, where a range of plausible T_2 ranging from 100 ms (blue lines/star) to 500 ms (red lines/star) in steps of 25 ms are investigated. Figs 1(a) and (c) illustrate the *x*- and *y*-components of the transverse magnetization produced by a 40 ms 4 Hz off-resonance pulse over a range of B_1 representative of that present in surface NMR. Figs 1(b) and (d) illustrate the *x*- and *y*-components of the transverse magnetization produced by an example adiabatic excitation pulse that is described by a 52.2 ms sweep over 100 Hz where the shape of the frequency sweep is determined using the numerically optimized modulation (NOM) approach (Ugurbil *et al.* 1988). A further discussion about the details of this example NOM pulse are given in Grombacher (2018); the investigated NOM pulse provides a good balance between a reasonable pulse duration, satisfactory depth resolution, and enhanced signal amplitudes for typical surface NMR conditions. The colour of each profile corresponds to a particular T_2–$T_{2\mathrm{IH}}$ pair in Fig. 1(e). Note that all investigated scenarios in Fig. 1 correspond to T_2^* of 80 ms. Each point in the profiles is formed by solving the Bloch equation using a fourth-order Runge–Kutta solver given the relevant B_1 amplitude, pulse waveform, T_2–$T_{2\mathrm{IH}}$ pair, a 5 ms deadtime, and an initial condition described by a unit magnetization at equilibrium. The Runge–Kutta solver allows the magnetization at time t_{i+1} to be predicted based on the magnetization at time t_i and the change in the magnetization over each time step (which is described by the Bloch equation). The magnitude of $T_{2\mathrm{IH}}$ is used to define the width of a Lorentzian B_0 distribution (Chen *et al.* 2005). Further discussion about how the B_0 distribution is included in the determination of the net m_x and m_y components is given in Grombacher *et al.* (2017). Briefly, we assume that the impact of $T_{2\mathrm{IH}}$ is well-described by static-dephasing (Sukstanskii & Yablonskiy 2001), which assumes that the water molecules do not diffuse far enough to experience a significant variation in the B_0 field during the pulse duration. The static diffusion assumption will break down in the presence of strong pore-scale B_0 variations. T_1 is equal to T_2 in these examples. For the off-resonance pulse, the profiles track one-another closely in the low B_1 limit and again in the high B_1 limit. For $B_1 \sim$ 1e-7 T some differences are observed between the profiles, particularly the magnitude of the first positive and negative peaks as well as the location of the falling edge of the main low B_1 peak at ~3e-7 T. For the NOM pulse the profiles demonstrate more variability. For the x-component (Fig. 1b) the magnitude of the main peak displays a strong dependence on the relative T_2–$T_{2\mathrm{IH}}$ magnitudes, with the smallest T_2 producing the lowest amplitude peak. For the NOM pulse's y-component the profiles track each other more closely, with similar behaviour observed at the location of the main low B_1 peak as was seen for the off-resonance pulse. For smaller and larger T_2^* values the profiles demonstrate greater and lesser variation, respectively (not shown).

RESULTS

Synthetic sounding curves

The transverse magnetization profiles shown in Fig. 1 represent one component of the surface NMR forward model (the transverse magnetization term $m_\perp$ where $m_\perp = m_y + i m_x$). The observed signal amplitudes are affected by several additional factors such as the pulse current amplitude, subsurface conductivity structure, subsurface water content and T_2^* profiles, and the transmit/receive loop geometries. For a detailed description of the surface NMR forward problem readers are referred to Weichman *et al.* (2000). To gain insight into how much the signal amplitude and phase will vary depending on the relative magnitude of T_2 and $T_{2\mathrm{IH}}$ Fig. 2 presents

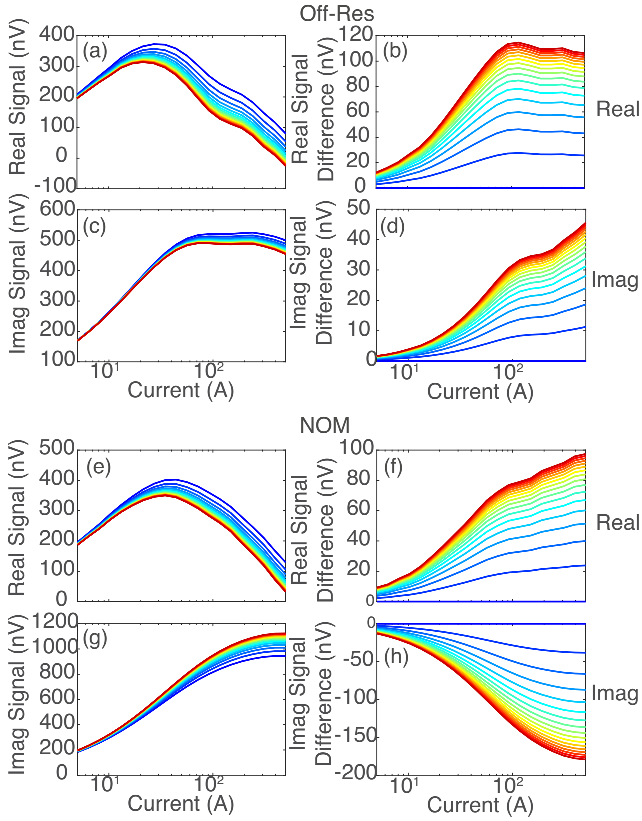

Figure 2. The top and bottom clusters of panels illustrate sounding curves that correspond to the same off-resonance and adiabatic pulse used in Fig. 1. The sounding curves correspond to synthetic surveys employing a 75 m circular loop, and a 50 Ωm 20 per cent water content half-space. (a) and (c) illustrate the real and imaginary sounding curves for the off-resonance pulse. (b) and (d) illustrate the difference between each sounding curve and the sounding curve for the small T_2 scenario (dark blue profiles in panels a and c). The difference represents the expected signal amplitude/phase variation due to differing T_2–$T_{2\mathrm{IH}}$ pairs. (e) and (g) illustrate the real and imaginary sounding curves for the adiabatic pulse. (f) and (h) illustrate the difference between each sounding curve and the sounding curve for the small T_2 scenario (dark blue profile in panels e and g). All sounding curves correspond to $T_2^* = 80$ ms, and the colours correspond to the same T_2–$T_{2\mathrm{IH}}$ pairs as in Fig. 1.

sounding curves that correspond to the same conditions investigated in Fig. 1. Sounding curves are formed by integrating the surface NMR kernel and represent a convenient metric to investigate the expected variation in signal amplitudes and phases. The sounding curves in Fig. 2 correspond to a 75 m circular coincident transmit/receive loop and 20 pulsed current amplitudes logarithmically sampled from 5 to 500 A. The subsurface is 50 Ωm 20 per cent water content half-space with a Larmor frequency of 2000 Hz and an inclination of 70°. The sounding curve colours again correspond to different T_2–$T_{2\mathrm{IH}}$ pairs (same colours as in Fig. 1). To produce the sounding curves for each scenario the transverse magnetization curves in Fig. 1 are used in the forward calculation. The sounding curves show the expected signal amplitudes at the end of a 5 ms dead time. Forward modelling is performed using MRSmatlab (Müller-Petke *et al.* 2016). The top and bottom clusters of Fig. 2 correspond to the 40 ms 4 Hz off-resonance pulse and NOM pulse, respectively. The left and right columns correspond to the sounding curves and the difference between each sounding curve and the shortest T_2 case, respectively. The difference plots are used to highlight the magnitude of the signal variation. At the right of each row the label indicates whether the sounding curves correspond to the real or imaginary signal. Consider first the off-resonance case, where the variation in the real component can be as large as 100 nV at larger currents in this example. Note that the real signal amplitudes in the large current limit are similar in magnitude to this level of variation (i.e. both (a) and (b) show up to ∼100 nV signals in the large current limit). This highlights that significant real amplitude perturbations can be induced depending on which T_2–$T_{2\mathrm{IH}}$ pair is present. The imaginary component shows a similar trend, but with the magnitude of variation being reduced compared to the real component. For the NOM pulse case (bottom cluster of Fig. 2), the real and imaginary signal amplitudes also demonstrate significant variation (highlighted by the large amplitudes in the difference plots (Figs 2f and h)). The signal differences approach ∼15–25 per cent of the signal amplitude, with positive and negative differences for the real and imaginary components, respectively. This indicates that significant phase variations are likely to occur in addition to the amplitude variations. The magnitude of the differences can also be used to define noise levels where it may be possible to differentiate between the different scenarios. If the noise level exceeds the magnitude of the signal differences it will be difficult to distinguish between the scenarios. Although the magnitude of signal variation will in practice depend on a number of factors such as the particular pulse used, the subsurface water content profiles, and the magnitude of T_2^* and T_2, Fig. 2 provides useful insight into the magnitude of potential signal variations.

In summary, Fig. 2 demonstrates that significant signal variations can be expected depending on the true T_2–$T_{2\mathrm{IH}}$ pair. That is, given a particular T_2^* observation the underlying T_2^*–T_2 pair can have a significant impact on the observed signal amplitude and phase. The hypothesis we wish to test is whether this signal variation can be exploited to gain insight into the T_2^*–T_2 relationship.

Synthetic tests to constrain the T_2^*–T_2 relationship

To constrain the relationship between T_2^* and T_2 we propose to conduct a parameter search involving multiple inversions of a data set, each time using a forward model that solves the full-Bloch equation with a distinct but plausible T_2–$T_{2\mathrm{IH}}$ pair consistent with the observed T_2^* value. The resulting data fits for the suite of inversions will be compared and the inversions that produce satisfactory data fits will be used to define the range of plausible T_2 estimates. Inversions that produce poor data fits will be used to determine the range of T_2 estimates inconsistent with the observed data. Effectively, we intend to use the impact of RDP effects (i.e. the signal and phase variation observed in Fig. 2) to encode the signal with information about the true T_2^*–T_2 relationship. To heighten sensitivity, we propose to jointly invert two data sets, one collected using an on-/off-resonance excitation pulse and a second collected using an adiabatic half passage pulse. The scheme is motivated by a desire to exploit the opposite sensitivities to RDP effects displayed in Fig. 2, where the differences in Figs 2b, d, and f are all positive as you move from blue to red (i.e. from small T_2 to large T_2) while the differences in Fig. 2(h) are negative as you move from blue to red. These differences stem from the different trajectories followed by the magnetization during on-/off-resonance and adiabatic excitation. For example, at large B_1 the adiabatic pulse quickly rotates the magnetization into the transverse plane thus exposing the m_x component (imaginary signal) to T_2 relaxation for an extended period. This causes the imaginary component of the adiabatic signal to

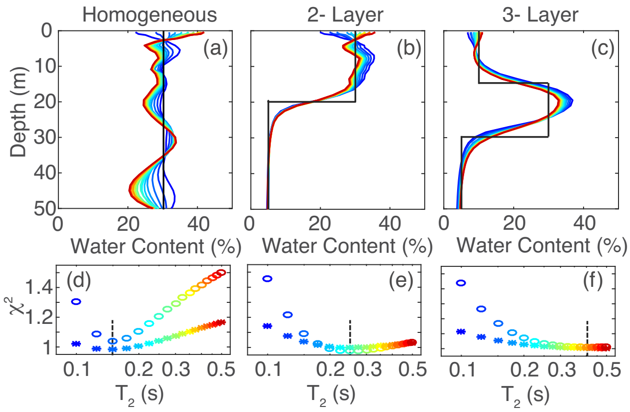

Figure 3. Estimated water content profiles (top row) and the corresponding data fits (bottom row) for a range of inversions each employing a plausible T_2 estimate based on the observed $T_2^* = 80$ ms. Each colour corresponds to the same T_2–$T_{2\mathrm{IH}}$ pairs shown in Fig. 1. Each column corresponds to a particular water content profile, where the true profile is shown by the black line in each case. The true T_2 value used to forward model the synthetic data in each case is indicated by the vertical dashed line in the bottom row. The stars and circles in the bottom row correspond to the real and imaginary data fits, respectively. Note that the χ^2 curves form a distinct minima that form around the true T_2 value.

display the opposite dependence. If T_2 is small the signal attenuation is greatest, while if $T_{2\mathrm{IH}}$ is small the adiabatic pulse can maintain coherence and thus displays little signal loss.

Fig. 3 illustrates three examples where the proposed framework is used to investigate if the T_2^*–T_2 range can be constrained from FID-only data. In each case, synthetic data are forward modelled for a survey geometry described by a 75 m circular coincident transmit/receive loop, 20 current amplitudes logarithmically sampled from 5 to 500 A, an inclination of 70°, and a 50 Ωm half-space. The water content profile is different for each column in Fig. 3, shown by the solid black line in each case. Gaussian noise with a standard deviation of 50 nV is added to all synthetic data prior to inversion. In all cases the true T_2^* is 80 ms, while the true T_2 varies in each of the columns (T_2 is 150 ms, 250 ms, and 400 ms in the left, centre, and right columns respectively, shown by the dashed black line in each case). Each column is given a different T_2 to investigate if the approach displays a strong sensitivity to the true T_2 value. T_1 is set equal to T_2 in all cases. The same T_2^* and T_2 value are present in the entire subsurface. The synthetic data set in each case is formed using both a 4 Hz off-resonance 40 ms pulse and an example NOM adiabatic pulse (the same pulses investigated in Figs 1 and 2). The complex-valued QT-inversion inversion is used in all cases (Müller-Petke & Yaramanci 2010), where a single exponential T_2^* value is fit within each depth layer. Forward modelling/inversion is performed using MRSmatlab (Müller-Petke *et al.* 2016).

Consider first the left column of Fig. 3, which corresponds to a 30 per cent water content half-space. In this example, where T_2^* is 80 ms (which can be determined directly from the synthetic data) the plausible range of T_2 can be constrained to values greater than 80 ms. To possibly narrow this range a parameter search is conducted where inversions are performed using forward models that consist of different but plausible T_2–$T_{2\mathrm{IH}}$ combinations each consistent with $T_2^* = 80$ ms (i.e. one forward model per star location in Fig. 1e). The same data set is inverted in each case. Examining the data misfits, which are represented in Fig. 3(d) as the χ^2 values for the real (stars) and imaginary (circles) data misfits, demonstrates that the data misfit is best when the forward model is given an accurate T_2 estimate. The χ^2 curves show a distinct minima around the true T_2 (dashed black line), where when the T_2 is underestimated (dark blue) or over-estimated (turquoise to red) the data fits are poorer. In this case, the plausible T_2 range can be tightly constrained around the true T_2. Note that the water content profile in Fig. 3(a) is also most accurately estimated when the forward model is given a reliable T_2 estimate (light blue profile). Consider next the centre column, which corresponds to a two-layer system representative of an unconfined aquifer underlain by a lower water content layer. In this case T_2^* is again equal to 80 ms, and the true T_2 is 250 ms. The same noisy synthetic data set is inverted using a suite of forward models each given a plausible T_2 estimate. The data misfits in this example (Fig. 3e) are large for the smallest T_2 estimates (blue), decreasing to a minimum around the true T_2 value (dashed line) and then slowly increasing for larger T_2 estimates. The slope of the χ^2 curves in this example is not as steep for overestimated T_2 as it is for underestimated T_2. In the final example (right column) the water content profile is described by a 3-layer system representative of a 15 m thick aquifer present in a low water content background. In this case, T_2^* is again equal to 80 ms but T_2 is now 400 ms. The data misfits in this case (Fig. 3f) show a similar trend as in the previous 2-layer example, where the χ^2 curves show poor data misfits at the smallest T_2 estimates (blue) with the data fit flattening out in the long T_2 limit. In this case, there is no distinct minima centred on the true T_2 (i.e. T_2 estimates of 300–500 ms produce effectively equivalent data fits) but the plausible range can be significantly narrowed from $T_2 > T_2^* = 80$ ms to $T_2 > \sim 300$ ms. The water content profiles in Figs 3(b) and (c) all consistently estimate the true water content profile well, but in practice only profiles that correspond to satisfactory data fits should be trusted. Overall, Fig. 3 demonstrates that the proposed protocol that involves adjusting the forward model to describe multiple plausible scenarios can likely be used to help further constrain the T_2^*–T_2 relationship.

To highlight the benefits of employing multiple pulse types (e.g. an adiabatic pulse and an off-resonance pulse as in Fig. 3), Fig. 4 illustrates the χ^2 curves produced for the same conditions investigated in Fig. 3 except where we consider the cases where only one pulse type is used. The top, middle and bottom panels of Fig. 4 correspond to the same subsurface conditions as in the left, centre and right columns of Fig. 3, respectively. The blue, red, and black profiles correspond to the results of the parameter search that employ a single NOM pulse, a single 40 ms 4 Hz off-resonance pulse, and both a NOM pulse and a 40 ms 4 Hz off-resonance pulse, respectively (same pulses as in Fig. 3). Note that the black profiles for the combined case are identical to those shown in the bottom row of Fig. 3. In all three cases, the blue and red profiles are consistently much flatter than the black profiles, and do not show clear minima at this noise level. The significantly increased steepness of the black profiles indicates that the proposed method is better suited to working with multiple pulse types simultaneously.

Note that the steepness of the minima in the χ^2 curves observed in Fig. 3 was different in each of the scenarios. In practice the sensitivity to the true T_2 (i.e. steepness of the minima) will depend on several factors, such as the true water content profile, the true T_2^* and T_2 values, and the noise levels. To highlight the role that these factors play in determining the effectiveness of the proposed protocol to constrain the range of plausible T_2 Fig. 5 illustrates the χ^2 curves for several examples. In all cases, T_2^* is again set to 80 ms and $T_2 = T_1$ in all cases. In Fig. 5(a), the true T_2 is set to 250 ms and 50 nV of Gaussian noise is added to the data. The dashed and solid lines correspond the real and imaginary χ^2 curves, respectively.

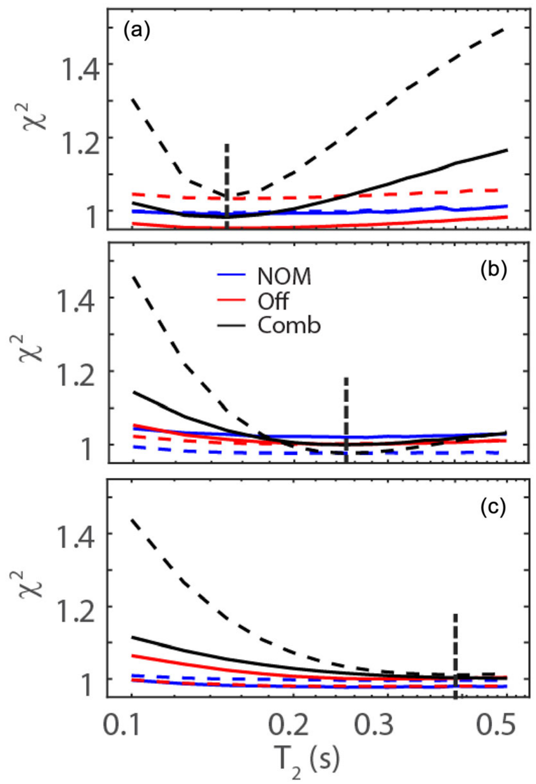

Figure 4. The data fits for a range of inversions each employing a plausible T_2 estimate based on observed $T_2^* = 80$ ms. (a)–(c) correspond to the same subsurface conditions as in the left, centre and right columns of Fig. 3. The blue and red lines correspond to data fits produced by a parameter search that employs a single pulse type (blue = NOM pulse, red = off-resonance pulse). The black line shows the data fits for the case where both pulse types are considered simultaneously. Solid and dashed lines correspond to real and imaginary data fits, respectively. The vertical dashed line shows the true T_2 in each case.

The curve colours in Fig. 5(a) correspond to the particular water content profile in each case, where black, blue, and red correspond to the water contents profiles in the left, centre, and right columns of Fig. 3. Note that the steepnesses of the minima differ depending on the water content profile, where the half-space model (black) shows a much deeper minima than the 3-layer case (red). This highlights that the effectiveness of the approach will display a strong sensitivity to the local water content profile. Consider next the impact of the noise level, where Fig. 5(b) illustrates the χ^2 curves for four different noise levels (colours). The true T_2 is 250 ms in this case and the water content profile is described by the 2-layer model in Fig. 3. The noise level plays a strong impact on the steepness of the minima, where the low noise limit show extremely poor data fits for inaccurate T_2 estimates. At higher noise levels the minima flattens, where in the high noise case (100 nV) only the imaginary χ^2 curve shows a small rise at small T_2. In this 100 nV case, the plausible range of T_2 cannot be narrowed to the same extent as in the lower noise cases. In Fig. 5(c), the true value of T_2 is now varied (colours). In this case, 50 nV of noise is added to the synthetic data and the water content profile is described by the two-layer model in Fig. 3. Fig. 5(c) highlights that the steepness of the minima will also display a strong sensitivity to the true T_2 value, where in this example the minima is much flatter for the low T_2 case (black) than in the large T_2 case (red). In Fig. 5(d), the value of T_2^* is now varied (colours). In this case, 50 nV of noise is added to the synthetic data,

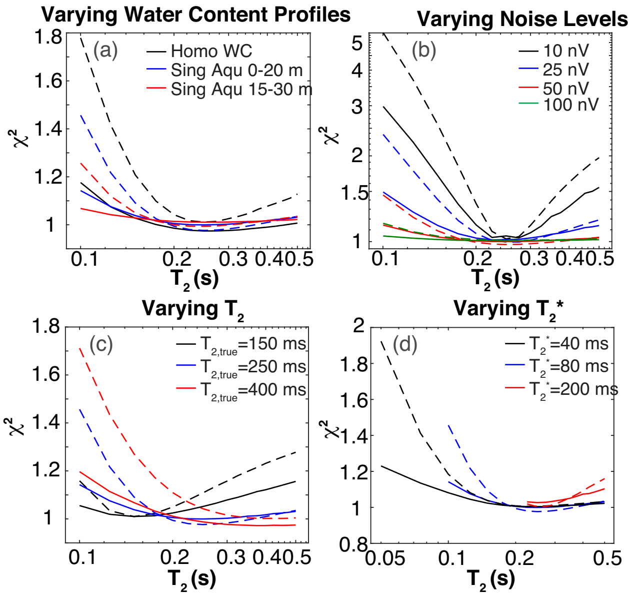

Figure 5. Real (solid) and imaginary (dashed) χ^2 curves illustrating the data fits produced for inversions conducted for a range of plausible T_2 scenarios for a suite of different conditions. (a) χ^2 curves for three different water content profiles (colours, and the same profiles as those in Fig. 3) for synthetic data that are forward modelled with $T_2^* = 80$ ms, $T_2 = 250$ ms and with 50 nV of noise added. (b) χ^2 curves for four different noise levels (colours). The underlying noise-free synthetic data is the same in each case, and is produced with $T_2^* = 80$ ms, $T_2 = 250$ ms and with the water content profile in Fig. 3(b). Note that the y-axis is logarithmic in (b). (c) χ^2 curves for three different synthetic data sets each forward modelled using a different T_2 (colours). The water content profile is the same as in Fig. 3(b), $T_2^* = 80$ ms, and 50 nV of noise is added. (d) χ^2 curves for three T_2^* values (colours). In each case, the water content profile is the same as in Fig. 3(b), $T_2 = 250$ ms, and 50 nV of noise is added.

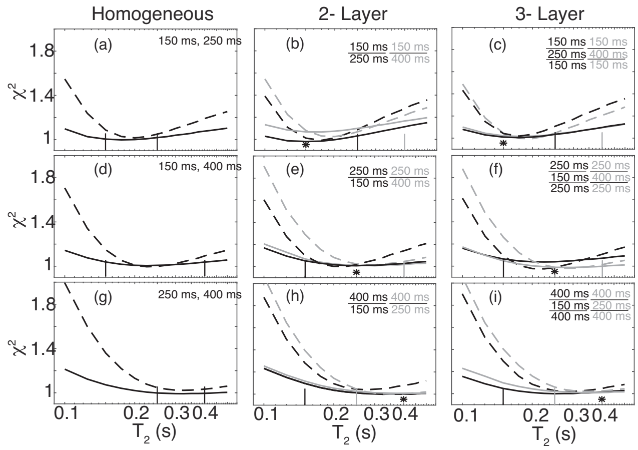

Figure 6. Real (solid) and imaginary (dashed) χ^2 curves illustrating the data fits produced for inversions conducted for a range of plausible T_2 scenarios for a suite of different conditions where multiple T_2 are present in the subsurface. In all cases the subsurface is a 50 Ωm 30 per cent water content half space with $T_2^* = 80$ ms. In the left column, two T_2 values are present in all depth layers (indicated by the legend and vertical lines in a, d and g). In the centre column, the subsurface is described by two layers with a boundary at 20 m depth. The upper and lower layers are each given a different T_2 value (see legends). The T_2 in the upper layer is indicated by the star, while the T_2 in the lower layer is indicated by the vertical lines. Two cases are investigated in each panel, grey and black curves each correspond to a particular T_2 in the lower layer. In the right column, the subsurface is described by three layer system with boundaries at 15 m and 30 m depth. The top and bottom layer are given the same T_2 in each case, while the middle layer is given a different T_2 (colour). The T_2 in the top and bottom layer is indicated by the star, while the T_2 in the middle layer is indicated by the vertical dashed lines. Two cases are investigated in each panel, grey and black curves each correspond to a particular T_2 in the middle layer (see legend).

the true $T_2 = 250$ ms, and the water content profile is described by the 2-layer model in Fig. 3. Fig. 5(d) highlights that the steepness of the minima will also depend on the T_2^*–T_2 contrast, where even in the long $T_2^* = 200$ ms (red) example the plausible range can be narrowed by noting the reduced data fit at longer T_2. Note that the coloured lines in each case begin at different T_2, this is because the plausible T_2 range can always be constrained to be larger than T_2^*. Taken together, Fig. 5 highlights that the effectiveness of the approach (i.e. steepness of the minima) will depend on several site dependent factors. However, a consistent ability to constrain the range of plausible T_2 is observed for a range of conditions.

Figs 3 and 5 considered synthetic models where the entire subsurface was given the same underlying T_2, in practice it is common that multiple T_2 present are present within a single depth layer or to encounter layers of contrasting T_2. To test the performance of the proposed method under conditions with multiple T_2 consider Fig. 6, which presents χ^2 curves produced using the same workflow as in Figs 3 and 5. The survey geometry/parameters and noise levels used in Fig. 3 are again used in Fig. 6. Note that Fig. 6 displays results where the true subsurface contains multiple T_2 values, but the forward model assumes that the same T_2 value (i.e. a single T_2 value) is present at all depths. In the left column of Fig. 6 the subsurface is a 50 Ωm 30 per cent water content half-space, where two T_2 values are present at all depths in equal abundances. Figs 6(a), (d) and (g) correspond to subsurfaces with T_2 equal to [150 250] ms, [150 400] ms and [250 400] ms. The true T_2 in each case are shown by the black vertical lines. In each case a distinct minima forms at the midpoint between the two true T_2 values (i.e. between the two vertical lines). At the minima a quality data fit is produced, and a T_2 estimate is produced that is representative of the rough average of the multiple T_2 present in the layer. Consider next a two-layer scenario (centre column of Fig. 6), where the subsurface is again described by a 50 Ωm 30 per cent water content half-space, but where the top 20 m is given a different T_2 than depths below 20 m (a single T_2 is present in each layer). The legends in Figs 6(b), (e) and (h) illustrate the T_2 values in the upper and lower layers, respectively. Each panel illustrates two pairs of χ^2 curves, each with the same T_2 in the upper layer (indicated by the star) but differing T_2 in the lower layer (indicated by the vertical lines). Fig. 6(b) shows a distinct minima forming at values slightly higher than the T_2 value in the upper layer (star). The presence of the second T_2 at depths below 20 m appears to slightly shift the minima towards the T_2 values at depth. Note that the $T_2 = 400$ ms case (grey) shifts the minima to higher values than the $T_2 = 250$ ms case (black). Figs 6(e) and (h) demonstrate similar trends, where the location of the minima is closest to the value of the T_2 in the upper layer (star), but is shifted slightly towards the values in the lower layer (observed by noting that the minima in the coloured curves are pulled slightly towards the relevant vertical line). Similar to the homogeneous case, the proposed workflow seems to consistently provide a quality data fit, while also estimating a representative average T_2 where the average seems to favour the shallow layer. The right column of Fig. 6 illustrates examples for a 3-layer scenario, where the subsurface is again a 50 Ωm 30 per cent water content half-space but where 3 layers from 0 m – 15 m, 15 m – 30 m, and below 30 m are each given a single T_2 value. The legends in Figs 6(c), (f) and (i) illustrate the relevant T_2 values, where in each case layers 1 and 3 are given the same T_2 values (indicated by stars) and layer 2 is given a distinct T_2 (indicated by the vertical lines). Each panel illustrates two scenarios where the T_2 in layer two is varied (colours). Similar behaviour is observed as in the two-layer case. The location of the minima is closest to the T_2 in the upper layer (star) while being pulled slightly towards the value in layer two (relevant vertical line). Considering all three cases together indicates that the proposed workflow, although based on a simplified assumption that treats all depths with the same T_2 and T_2^* value, is able to produce quality data fits and reliable estimates of a representative T_2 value that tends to favour the true T_2 values at shallow depths.

Field feasibility tests

To verify the feasibility of the proposed method in practice a field data set was collected at a site near Leque Island, Washington using the GMR system. The survey employed a two-turn 42 m circular coincident loop, a 40 ms on-resonance pulse and a NOM adiabatic pulse (same NOM pulse as in the previous synthetic cases). The conductivity structure at the site is known from a previous EM survey and is included in the forward modelling. Both the on-resonance and NOM data sets each include 36 pulse moments sampled logarithmically from ~1.75 to ~296 A. The Larmor frequency at the site was observed to be 2290 Hz. Prior to inverting the two data sets jointly, a phase correction is applied to each individual data set. This is required because current processing practices impart an additional phase on the data. This phase is typically referred to as the instrument or processing phase, and is related to filter bandwidths, the pulse waveforms, and dead times. This processing phase is constant across all pulse moments, that is, the on-resonance and NOM data sets are each given a single-phase correction. The procedure used to calculate this instrument phase is discussed in Grombacher *et al.* (2016).

The T_2^* at the site was observed to be consistently ~30 ms across all pulse moments. Using this value the plausible range of T_2 can be constrained to greater than ~30 ms. To narrow this range a parameter search is conducted where the data is inverted using a suite of forward models each containing a distinct but plausible T_2 estimate with T_2^* equal 30 ms; T_2 estimates of 50 ms (blue), 100, 150, 200, 300, 400 and 500 ms (red) are investigated. All depths in the forward model are given the same T_2^* and T_2 value in this example. T_1 is also set equal to T_2. Comparing the data fits in each case (i.e. the χ^2 curves in Fig. 7c) demonstrates that forward models given small T_2 estimates (e.g. T_2 of 50 ms and 100 ms) produce poor data fits, while longer T_2 estimates provide more robust data fits. A minima appears to form around a T_2 estimate of 250 ms, with the χ^2 curves flattening out at higher T_2 estimates. The corresponding water content profiles in each case are shown in Fig. 7(a), where the profiles for large T_2 all produce similar results. The estimated T_2^* profiles (not shown) show little structure and are consistently near the $T_2^* = 30$ ms estimate used by the forward model. From Fig. 7(c), it is likely that the plausible range of T_2 can be constrained from values > T_2^*~30 ms to a smaller range where T_2 > ~150/200 ms, with the best estimate corresponding to $T_2 = 250$ ms.

To investigate if this estimated T_2 range is reasonable we compare against a T_2 log produced using the Vista Clara Javelin tool that was conducted in the centre of the surface NMR survey. The logging T_2 estimates are considered the true T_2 value in this case

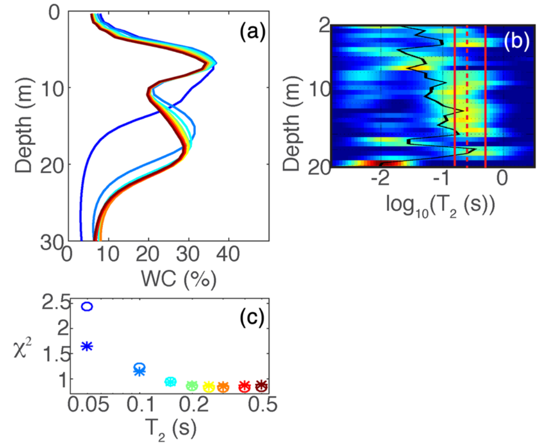

Figure 7. Field test of the proposed workflow to constrain the T_2^*–T_2 relationship. (a) Estimated water content profiles for a range of inversions each conducted with a distinct but plausible T_2 estimate. The relevant T_2 for each colour is indicated in (c). (b) A T_2 log produced at the site using the Javelin tool. Cold and hot colours correspond to regions with low and high water content, respectively. The two solid red lines highlight the 150–500 ms range where the satisfactory data fits are produced for the surface NMR data, while the dashed red line corresponds to the best data fit that estimated $T_2 = 250$ ms. (c) The χ^2 curve showing the data fit for each T_2 estimate. Stars and circles correspond to the real and imaginary data fits, respectively.

given that the logging measurement is capable of direct T_2 measurements at a high vertical resolution. The logging T_2 values are used as the reference against which the accuracy of the surface NMR FID-based T_2 estimate will be judged. The T_2 log (Fig. 7b) consistently exhibits values in the range from ~150 ms to 500 ms, which corresponds to the bright (green/yellow) regions. The vertical red lines are placed at T_2 of 150 ms and 500 ms, and serve to highlight that the surface NMR FID-only based T_2 estimate of T_2 > ~150 ms with a best guess of $T_2 = 250$ ms (dashed red line) agrees quite well with the logging result, representing an averaged value similar to the behaviour observed in Fig. 6. The T_2 log demonstrates more variability, including values less than 150 ms at certain depths (e.g. 5–8 m and 20 m depth) but over the full depth interval the T_2 log agrees well with the FID-only based estimate. The surface NMR measurement is also expected to be less sensitive to the fastest relaxation times observed in the logging NMR measurement (e.g. the ~15–25 ms T_2 present from 5–8 m depth) because of the typical pulse durations and dead times in surface NMR.

To illustrate the data quality and goodness of fit Figs 8(a) and (c) show the measured real and imaginary data, respectively. The reason for the sharp horizontal contrast at a q index of 36 is because this represents the switch from the on-resonance to NOM data (i.e. q indices 1 to 36 correspond to on-resonance data while indices 37 to 72 correspond to NOM data). Figs 8(b) and (d) illustrate the forward modelled data corresponding to the inversion that used a T_2 estimate of 250 ms, which provided the best data fit. Note that the modelled data accurately reproduces the observed data set reliably capturing the positive and negative lobes in the real and imaginary components, and providing a high-quality fit to both the on-resonance and adiabatic data while using the same water content profile. To further demonstrate the level of data fit for various inversions that used different T_2 estimates Fig. 9 illustrates the real and imaginary data misfits for the inversions that used T_2 estimates of 50, 150, 250 and 400 ms. In the left column (T_2 estimate of 50 ms), significant structure remains in the data misfit plots highlighting that

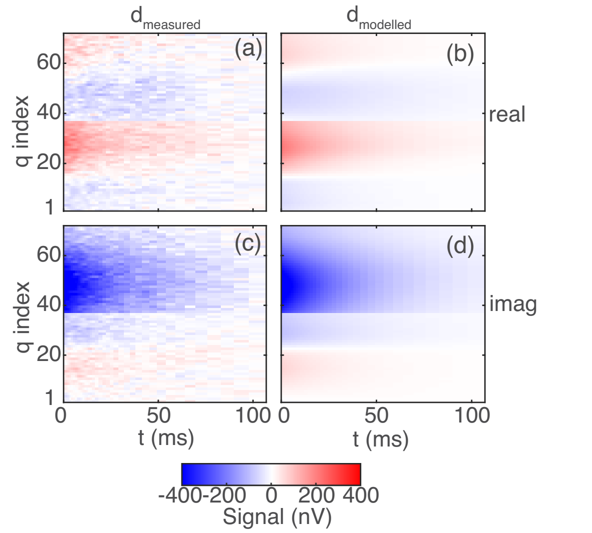

Figure 8. The measured (left column) and modelled (right column) data that corresponds to the $T_2 = 250$ ms water content profile in shown Fig. 7. The total data set contains both off-resonance data (q indices 1–36) and adiabatic pulse data (q indices 37–72). The top and bottom rows show real and imaginary data, respectively. Each panel uses the same colour bar.

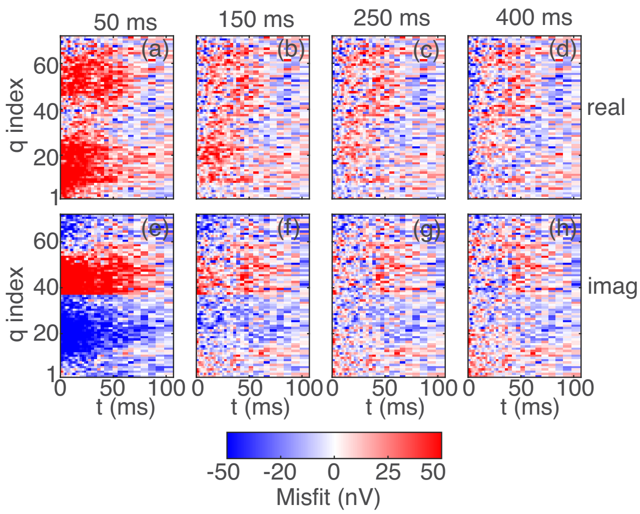

Figure 9. Data misfits corresponding to four of the water content profiles shown in Fig. 7. Each column corresponds to an inversion result that corresponds to a different T_2 estimate (relevant T_2 stated at top of column). The selected T_2 range extends from below to above the minima location in Fig. 7(c). The $T_2 = 250$ ms column corresponds to the data shown in Fig. 8. The top and bottom rows show the real and imaginary data fit, respectively. All panels use the same colour bar. A quality data fit is described by random red/blue behaviour, consistent strong structure indicates a poor data fit.

the inversion in this case struggles to fit the observed data. Note the positive/negative lobes in the imaginary misfit (Fig. 9e), which arise due to the differing sensitivity of the on-resonance and NOM pulse (i.e. the positive versus negative trends shown by the sounding curves in Fig. 2d and h). The data fit is improved for the $T_2 = 150$ ms case, but a small positive/negative lobe structure remains in the imaginary component, as well as a red structure at $t \sim 30$ ms in the real component. For longer T_2 (250 ms and 400 ms) the data misfit is further improved, with the misfits showing no significant structure and a misfit level consistent with the observed noise level of ∼25 nV. Note also that the colour bar limits in Fig. 9 are eight times smaller than in Fig. 8. Overall, the ability to fit the complex valued data using a limited range of plausible T_2 estimates and that this narrower range matches well with logging T_2 measurements at the site demonstrates the feasibility of the proposed method to help constrain the T_2^*–T_2 relationship using only FID data.

DISCUSSION

RDP effects manifest in different ways depending on the particular excitation pulse used (Hadjuk *et al.* 1993) and the relative magnitude of T_2 and $T_{2\mathrm{IH}}$, which can lead to significant perturbation on the surface NMR signal's amplitude, phase, and spatial origin. Employing a forward model that solves the full Bloch equation with appropriately weighted relaxation terms provides the forward model the flexibility to more accurately weight the RDP effects. The magnitude of signal amplitude/phase variation for different T_2–$T_{2\mathrm{IH}}$ scenarios suggests that forward models that do not adapt the excitation modelling to local conditions (i.e. always solve the same Bloch equation, as is the standard in surface NMR) may struggle to reliably describe the complex surface NMR signal in some situations. We hypothesize that this may be a contributing factor to challenges producing satisfactory data fits using the complex inversion in certain conditions. The results of the field study support this hypothesis, demonstrating that modelling RDP for varying T_2^*–T_2 relationships can help to improve the fit to complex-valued surface NMR data. The results are also consistent with Irons & Li (2014), where it was shown that the standard surface NMR forward model struggled to fit complex-surface NMR data at several sites containing strong magnetic field inhomogeneity. In the Irons & Li (2014) study, a forward modelling approach that accounts for non-exponential decays was observed to improve data fit.

Figs 3–7 indicate that when the updated forward model is paired with a framework that performs a parameter search involving multiple inversions for various plausible T_2 scenarios valuable insight into the true T_2^*–T_2 can be extracted from FID-only data. Figs 3–7 demonstrate the potential of this workflow, where an alternative modelling/inversion framework is shown to greatly enhance the value of an FID-only data set. Without the ability to further constrain the T_2^*–T_2 relationship, the utility of FID data for estimation of pore-size/permeability is plagued by the large uncertainty about the reliability of T_2^*-based estimates. For example, in the presented field study where T_2^*∼30 ms is observed, if it was assumed that $T_2^* \sim T_2$ the resulting pore-size/permeability estimate would be very poor. Unfortunately, the standard modelling/inversion protocols are unable to diagnose that $T_2^* \sim T_2$ is a poor assumption in that case. However, using the updated forward model and the proposed framework allows one to gain insight into the true T_2^*–T_2 relationship in this case, and to determine that T_2^* is dominated by B_0 inhomogeneity effects at the site and that the true underlying T_2 is most likely in the $\sim >$150 ms range.

The proposed framework exploits the complex inversion, where real and imaginary data are treated separately. The standard inversion approach in surface NMR typically handles only amplitudes, referred to as an amplitude-only inversion. While the updated forward model can also be used in the context of the amplitude-only inversion, the proposed framework is best suited to complex-inversions. Tests performed using the amplitude-only inversion, where data were inverted for multiple plausible T_2 scenarios, demonstrated less sensitivity than the complex-inversion (i.e. the minima in the χ^2 curves were flatter). An added benefit of employing the complex inversion, beyond increasing sensitivity to the true T_2^*–T_2

relationship, is that the resolution benefits of complex-inversion can be exploited (Braun & Yaramanci 2005).

The effectiveness of the proposed workflow will depend on a number of site-specific parameters, such as the local noise levels, T_2^*, T_2, water content profiles and the types of pulses employed. We recommend that multiple pulse types be employed and the data inverted simultaneously. For tests where only a single pulse type was used a reduced sensitivity was observed (i.e. flatter minima). The complementary use of an on-/off-resonance pulse and an adiabatic excitation pulse appears to be well-suited to this approach. These two pulse types tend to display an opposite sensitivity in their imaginary components (observed by noting the opposite red to blue trends in Figs 2d and h). Evidence of the increased sensitivity of the imaginary component can be seen in all χ^2 profiles in Figs 3–7, where the imaginary component consistently displays steeper minima than the real component. We recommend that an off-resonance pulse be combined with an adiabatic excitation pulse. The advantage of choosing an off-resonance pulse over an on-resonance pulse is that it offers improved resolution (Grombacher *et al.* 2014), and allows the frequency-cycling method to be exploited to improve the accuracy of the forward model (Grombacher *et al.* 2016). Future work will further explore the potential combination of multiple pulse types/durations with the intention of heightening sensitivity to RDP encoding.

The proposed methodology uses a forward modelling scheme that solves the full Bloch equation, where the relaxation terms are weighted using T_2^* observations and T_2 estimates. The current workflow uses a simplified parameter search that assigns the entire subsurface a single T_2^* and T_2. Although these values are varied for subsequent inversions, they currently remain fixed during a single inversion. The reason this simplified approach is employed is that the goals of this study are to (1) demonstrate sensitivity of the signal amplitude/phase to the relative magnitude of the T_2 and $T_{2\mathrm{IH}}$ and (2) to explore if this sensitivity can be exploited to constrain the T_2^*–T_2 relationship. This type of approach is easily integrated into standard inversion workflows. To implement this approach it simply requires that the transverse magnetization (m_x and m_y) is specified as a function of the B_1 amplitude, thus allowing a lookup table to be used to populate the transverse magnetization component of the surface NMR forward problem. The m_x and m_y profiles for a particular pulse and T_2^*–T_2 pair are determined by solving the Bloch equation with appropriately weighted relaxation terms and B_0 distribution. The proposed workflow where multiple plausible T_2 scenarios are investigated effectively represents a parameter search where we have a reduced model space (i.e. the parameter we seek to constrain is a single T_2 present at all depths that ranges from T_2^* to $\sim$1 s). A more robust/flexible approach would be to build an inversion protocol where T_2 and T_2^* are allowed to vary for different depth layers, thus providing greater flexibility to account for spatial variability and more appropriately weight the relaxation terms in the Bloch equation in each depth layer. This type of an approach will require a non-linear inversion as the kernel must be recalculated after each iteration to reflect the current best estimate of the subsurface properties. Future work will focus on building this type of non-linear inversion, while also investigating if the data is capable of reliably constraining a depth-dependent T_2 inversion that uses only FID-data.

The proposed workflow intends to improve the information content of the FID measurement. It is not intended to replace the use of spin-echo or multi-echo measurements; these approaches still provide valuable insight into relative pore-sizes/permeability through their direct T_2 sensitivity. The advantage of the presented approach is that it improves the information content of the most widely implemented surface NMR measurement, one that corresponds to the shortest measurement times and greatest penetration depths. In practice, the spin-echo and multiecho measurements would serve as valuable complements to the proposed method likely allowing the T_2^*–T_2 relationship to be even further constrained. Note that FIDs also occur during the standard spin-echo and multiecho approaches (after each pulse), which suggests that the proposed workflow could be adapted to work with the FIDs produced during spin-echo and multi-echo measurements.

CONCLUSIONS

One of the primary shortcomings of the surface NMR FID measurement is the uncertainty surrounding the meaning of the relaxation time T_2^*. Ideally T_2^* can be used to provide valuable insight into pore-size/permeability, but an inability to determine whether the observed decay is controlled by T_2 processes or by dephasing limits the utility of T_2^*. If an incorrect assumption is made about the mechanisms controlling T_2^* it may lead to biased interpretations of the subsurface properties. To improve the utility of FID measurements, the relationship between T_2^* and T_2 must be better constrained. An approach involving a forward model that solves the full Bloch equation for a range of distinct but plausible T_2^*–T_2 scenarios is used in combination with the complex-inversion to help constrain the true T_2^*–T_2 relationship. Synthetic and field tests demonstrate that forward models employing poor estimates of the true T_2 struggle to accurately fit complex data, and that the range of T_2 estimates that produce reliable data fits can help to significantly narrow the plausible range of true T_2 value. We recommend that the approach combines multiple pulse types (e.g. an on-/off-resonance pulse and an adiabatic pulse). The current implementation that employs excitation modelling that assumes a single T_2^*/T_2 at all depths is shown to be capable of estimating representative T_2 values for relatively simple subsurfaces. Future work will focus on an improved inversion capable of estimating a depth-dependent T_2.

The proposed workflow exploits that RDP effects display a strong dependence on the relative contribution of T_2 and dephasing to T_2^*, which can have significant impacts on the signal amplitude, phase and spatial origin. This method effectively uses RDP effects to encode information about the underlying T_2^*–T_2 relationship in the signal amplitude and phase. The updated forward model provides the flexibility to more accurately weight RDP effects based on the current best estimate of subsurface properties. The approach is also likely to help improve the stability of the complex-inversion by providing a more robust ability to describe the signal phase.

ACKNOWLEDGEMENTS

DG was supported by funding from a Danish Council for Independent Research Postdoctoral Grant (DFF-5051-00002). The authors would like to thank Dr. Elliot Grunewald for collection of the surface NMR data. The NMR T_2 log was acquired by Vista Clara with funding from the U.S. Department of Energy under Grant DE-SC0004623. MRSmatlab was used to forward model/invert all synthetic and field surface NMR data (Müller-Petke *et al.* 2016).

REFERENCES

Braun, M. & Yaramanci, U., 2005. Study on complex inversion of magnetic resonance sounding signals, *Near Surf. Geophys.,* **3**(3), 155–163.

Brownstein, K.R. & Tarr, C.E., 1979. Importance of classical diffusion in NMR studies of water in biological cells, *Phys. Rev. A,* **19**(6), 2446–2453.

Chen, Q., Marble, A.E., Colpitts, B.G. & Balcom, B.J., 2005. The internal magnetic field distribution, and single exponential magnetic resonance free induction decay, in rocks, *J. Magn. Reson.,* **175**(2), 300–308.

Grombacher, D., 2018. Numerically optimized modulations for adiabatic pulses in surface nuclear magnetic resonance, *Geophysics,* **83**(2), JM1–JM14.

Grombacher, D., Walbrecker, J.O. & Knight, R., 2014. Imparting a phase during excitation for improved resolution in surface nuclear magnetic resonance, *Geophysics,* **79**(6), E329–E339.

Grombacher, D., Müller-Petke, M. & Knight, R., 2016. Frequency cycling for compensation of undesired off-resonance effects in surface nuclear magnetic resonance, *Geophysics,* **81**(4), WB33–WB48.

Grombacher, D., Behroozmand, A. & Auken, E., 2017. Accounting for relaxation during pulse effects for long pulses and fast relaxation times in surface nuclear magnetic resonance, *Geophysics,* **82**(6), JM23–JM36.

Grunewald, E. & Knight, R., 2011. The effect of pore size and magnetic susceptibility on the surface NMR relaxation parameter T_2^*, *Near Surf. Geophys.,* **9,** 169–178.

Grunewald, E. & Walsh, D.O., 2013. Multiecho scheme advances surface NMR for aquifer characterization, *Geophys. Res. Lett.,* **40**(24), 6346–6350.

Grunewald, E., Knight, R. & Walsh, D., 2014. Advancement and validation of surface nuclear magnetic resonance spin-echo measurements of T_2, *Geophysics,* **79**(2), EN15–EN23.

Hadjuk, P.J., Horita, D.A. & Lerner, L.E., 1993. Theoretical analysis of relaxation during shaped pulses. I. The effects of short T_1 and T_2, *J. Magn. Reson. A,* **103**(1), 40–52.

Howard, J.J. & Kenyon, W.E., 1992. Determination of pore size distribution in sedimentary rocks by proton nuclear magnetic resonance, *Mar. Pet. Geol.,* **9**(2), 139–145.

Irons, T.P. & Li, Y., 2014. Pulse and Fourier transform surface nuclear magnetic resonance: comprehensive modelling and inversion incorporating complex data and static dephasing dynamics, *Geophys. J. Int.,* **199**(3), 1372–1394.

Kenyon, W., Day, P., Straley, C. & Willemsen, J., 1988. A three-part study of NMR longitudinal relaxation properties of water-saturated sandstones, *SPE Formation Eval.,* **3**(3), 622–636.

Legchenko, A. & Valla, P., 2002. A review of the basic principles for proton magnetic resonance sounding measurements, *J. Appl. Geophys.,* **50**(1–2), 3–19.

Legchenko, A., Baltassat, J.M., Bobachev, A., Martin, C., Robain, H. & Vouillamoz, J.M., 2004. Magnetic resonance sounding applied to aquifer characterization, *Ground Water,* **42**(3), 363–373.

Legchenko, A., Vouillamoz, J.M. & Roy, J., 2010. Application of the magnetic resonance sounding method to the investigation of aquifers in the presence of magnetic materials, *Geophysics,* **75**(6), L91–L100.

Legchenko, A.V. & Shushakov, O.A., 1998. Inversion of surface NMR data, *Geophysics,* **63**(1), 75–84.

Mohnke, O. & Yaramanci, U., 2008. Pore size distributions and hydraulic conductivities of rocks derived from magnetic resonance sounding relaxation data using multi-exponential decay time inversion, *J. Appl. Geophys.,* **66**(3–4), 73–81.

Müller-Petke, M. & Yaramanci, U., 2010. QT inversion—Comprehensive use of the complete surface NMR data set, *Geophysics,* **75**(4), WA199–WA209.

Müller-Petke, M., Braun, M., Hertrich, M., Costabel, S. & Walbrecker, J., 2016. MRSmatlab—a software tool for processing, modeling, and inversion of magnetic resonance sounding data, *Geophysics,* **81**(4), WB9–WB21.

Schirov, M., Legchenko, A. & Creer, G., 1991. A new direct non-invasive groundwater detection technology for Australia, *Explor. Geophys.,* **22**(2), 333–338.

Straley, C., Rossini, D., Vinegar, H.J., Tutunjian, P.N. & Morriss, C.E., 1997. Core analysis by low-field NMR, *Log Analyst,* **38**(2), 84–94.

Sukstanskii, A.L. & Yablonskiy, D.A., 2001. Theory of FID NMR signal dephasing induced by mesoscopic magnetic field inhomogeneities in biological systems, *J. Magn. Reson.,* **151**(1), 107–117.

Ugurbil, K., Garwood, M. & Rath, A.R., 1988. Optimization of modulation functions to improve insensitivity of adiabatic pulses to variations in B_1 magnitude, *J. Magn. Reson.,* **80,** 448–469.

Walbrecker, J.O, Hertrich, M., Lehmann-Horn, J.A. & Green, A.G., 2011. Estimating the longitudinal relaxation time T_1 in surface NMR, *Geophysics,* **76**(2), F111–F122.

Weichman, P.B., Lavely, E.M. & Ritzwoller, M.H., 2000. Theory of surface nuclear magnetic resonance with applications to geophysical imaging problems, *Phys. Rev. E,* **62,** 1290–1312.